

Temporally Consistent Online Depth Estimation in Dynamic Scenes

Zhaoshuo Li^{1*}, Wei Ye², Dilin Wang², Francis X. Creighton¹, Russell H. Taylor¹,
Ganesh Venkatesh², Mathias Unberath¹

¹ Johns Hopkins University ² Reality Labs, Meta Inc.

Abstract

Temporally consistent depth estimation is crucial for real-time applications such as augmented reality. While stereo depth estimation has received substantial attention that led to improvements on a frame-by-frame basis, there is relatively little work focused on maintaining temporal consistency across frames. Indeed, based on our analysis, current stereo depth estimation techniques still suffer from poor temporal consistency. Stabilizing depth temporally in dynamic scenes is challenging due to concurrent object and camera motion. In an online setting, this process is further aggravated because only past frames are available. In this paper, we present a technique to produce temporally consistent depth estimates in dynamic scenes in an online setting. Our network augments current per-frame stereo networks with novel motion and fusion networks. The motion network accounts for both object and camera motion by predicting a per-pixel SE3 transformation. The fusion network improves consistency in prediction by aggregating the current and previous predictions with regressed weights. We conduct extensive experiments across varied datasets (synthetic, outdoor, indoor and medical). In both zero-shot generalization and domain fine-tuning, we demonstrate that our proposed approach outperforms competing methods in terms of temporal stability and per-frame accuracy, both quantitatively and qualitatively. Our code will be available online.

1. Introduction

For online applications such as augmented reality, estimating consistent depth across video sequences is important, as temporal noise in depth estimation may corrupt visual quality and interfere with downstream processing such as surface extraction. One way to acquire metric depth (*i.e.* without scale ambiguity) is to use calibrated stereo images. Recent developments in stereo depth estimation have been focusing on improving disparity accuracy on a per-frame basis [4, 6, 11, 24]. However, none of these approaches

considers temporal information nor attempts to maintain temporal consistency. We examine the temporal stability of different per-frame networks and find that current solutions suffer from poor temporal consistency, with one example shown in Fig. 1. Concisely, we observe that per-frame stereo networks predict inter-frame disparity changes that are significantly different compared to the ground truth (x -axis, $|\Delta d / \Delta d_{\text{gt}}|$). We quantify such temporal inconsistency in predictions across multiple datasets in Sec. 4 and provide qualitative visualization of resulting artifacts in the video supplementary material to further illustrate the case.

We posit that stabilizing depth estimation temporally requires reasoning between the predictions of current frame and previous frames, *i.e.* establishing cross-frame correspondences and correlating the predicted values. In the simplest case where the scene is static and camera poses are known/computed [13, 15], camera motion can be corrected by a single SE3 transformation. Given geometric constraints of multiple views [1], the aligned cameras have the same viewpoint onto the static scene and therefore, depth values of each pixel location are expected to be the same.

However, in a *dynamic* environment with moving and deforming objects, multi-view constraints do not hold. Even if

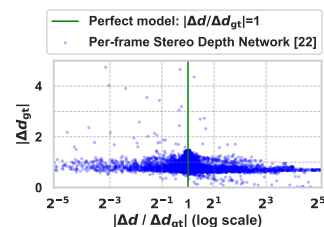


Figure 1. Illustration of temporal inconsistency of contemporary per-frame stereo networks. Let Δd_{gt} be the ground truth frame-to-frame disparity change when tracing the same points across time. The ratio of a stereo network’s prediction over ground truth $|\Delta d / \Delta d_{\text{gt}}|$ on the x -axis is plotted against the magnitude of ground truth $|\Delta d_{\text{gt}}|$ on the y -axis. The green vertical line represents a model with no temporal noise ($|\Delta d / \Delta d_{\text{gt}}| = 1$). Predicted inter-frame disparity change of the network is several orders larger or smaller than the ground truth disparity change.

*Work completed during internship at Reality Labs, Meta Inc.

cross-frame correspondences are established, independent depth estimates for corresponding points cannot simply be fused. This is because depth is not translation invariant and thus, fusion requires aligning depth predictions into a common coordinate frame. Therefore, prior work such as [10, 17] explicitly remove moving objects and only stabilize the static background to comply with the constraint, which restricts their applicability. Given additional 3D motion of each pixel, *e.g.* estimated by scene flow, depth of both moving and static objects can be aligned in the same coordinate frame, which then enables temporal consistency processing [33]. However, same as the previously mentioned approaches, [33] uses information from both past and future frames, and optimizes network parameters at application time, limiting itself to *offline* use.

In an *online* setting, there exist networks for temporally consistent depth estimation such as [5, 23, 32]. To incorporate temporal information, a recurrent network across time (LSTM or GRU) is appended to the depth estimation modules. However, these recurrent networks do not provide explicit reasoning between frames. Moreover, same as the above techniques, these approaches [5, 23, 32] consider depth estimation from single images, not stereo pairs. Due to the scale ambiguity of monocular depth estimation, prior work mainly focus on producing estimates with consistent scale across frames [10, 33] instead of reducing the inter-frame jitter that arises in stereo depth estimation.

Traditionally, to encourage temporal consistency in *metric depth* obtained from stereo cameras and RGBD sensors, prior techniques have relied on hand-crafted probability weights [19, 26, 29]. One such method is Kalman filter [29], which combines previous and current predictions based on associated uncertainties. However, it assumes that measurement error is Gaussian, which generally fails in our scenario due to occlusion and de-occlusion between frames.

In this work, we design an end-to-end network that produces temporally consistent depth estimation for dynamic scenes in an online setting. To account for inter-frame motion, we integrate a motion network that predicts a per-pixel SE3 transformation that aligns the previous frame’s estimates to the current frame. To remove temporal jitters and outliers from the estimates, a fusion network is designed to aggregate depth predictions based on past and current observations. Compared with existing methods, our approach produces temporally consistent metric depth and is capable of handling dynamic scenes in an online setting.

We evaluate our approach on varied datasets, including synthetic environments of rigid [20] or deforming [3, 28] objects, real-world footage of driving scenes [27], indoor and medical environments. Our approach consistently improves over competing approaches both with and without fine-tuning in terms of temporal metrics, by up to 63%, while performing on par in terms of per-frame accuracy.

The improvement is attributed to the temporal information that our model learns to leverage. We conduct extensive ablation studies of different components of our network. We further demonstrate the potential and performance upper bound of our proposed setup empirically, which may motivate future research to extend upon our work. Our network runs at 25 FPS on modern hardware.

2. Related Work

Rectified stereo depth networks compute disparity between left and right images to obtain the depth estimate given camera parameters. In recent years, deep learning-based algorithms have received substantial attention. Different network architectures have been proposed including 3D-convolution-based networks such as PSMNet [4], correlation-based networks such as HITNet [24], hybrid approaches with both 3D convolution and correlation such as GwcNet [6], and transformer-based networks such as STTR [11]. Our methods builds on top of these per-frame depth estimation methods to improve temporal consistency.

Temporally consistent depth networks aim to produce coherent depth for a video sequence. *Offline* approaches use some or all of the video frames, *i.e.* exploiting future frame information. Methods such as [13, 15] are only applicable in static scenes while others [10, 17] explicitly mask out moving objects and optimize for static background only. Zhang *et al.* [33] extend the aforementioned prior methods to dynamic scenes with moving objects by using additional 3D scene flow estimation. Different from the above offline approaches, our framework is designed for an *online* setting. *Online* approaches such as [23, 32] have used recurrent modules to aggregate temporal information. However, these approaches were studied in the context of monocular depth, where errors are dominated by scale inconsistency [10, 33]. Moreover, the recurrent modules do not provide an explicit mechanism of how temporal information is used. Our network is instead designed for metric depth from stereo networks and provides explicit reasoning between frames.

Scene flow estimation seeks to recover inter-frame 3D motion. Methods such as [18, 25, 30] recover motion from a set of stereo or RGBD images, while other methods such as [2, 14] operate directly on point clouds to estimate the 3D scene flow. While previous algorithms aim at generating accurate scene flow between frames, our work uses the 3D motion as an intermediary such that previous depth estimates can be aligned with the current scene. Following RAFT3D [25], we predict the inter-frame 3D motion as a per-pixel SE3 transformation map.

Simultaneous localization and mapping (SLAM) jointly estimates camera poses and a mapping of the scene. Many approaches [8, 16, 21, 31], such as DynamicFusion, accumulate information over all past frames. These approaches may include objects that have already exited the

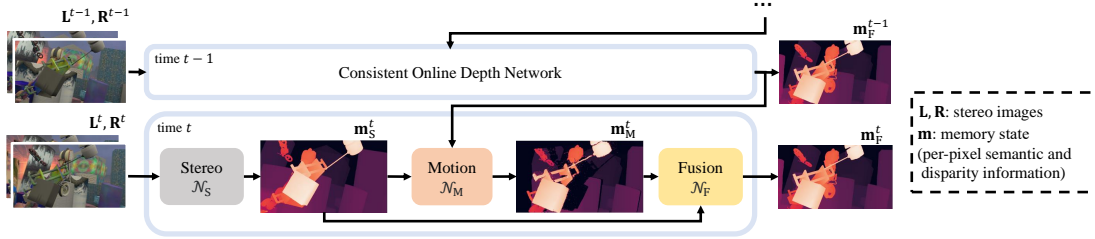


Figure 2. Overview of our temporally consistent online depth estimation network, showing the information flow between successive frames. Our network has three sub-networks: *stereo* (S), *motion* (M) and *fusion* (F) networks. Each sub-network extracts or updates a memory state \mathbf{m} , which is a combination of semantic and disparity information. Given an input video sequence, the stereo network \mathcal{N}_S extracts the feature and disparity on a per-frame basis from the stereo images $\mathbf{L}^t, \mathbf{R}^t$, forming the initial memory state \mathbf{m}_S^t at current time t . The motion network \mathcal{N}_M then transforms the preceding memory state \mathbf{m}_F^{t-1} to the current scene, generating the aligned memory state \mathbf{m}_M^t . A fusion network \mathcal{N}_F lastly fuses the aligned disparity from $t - 1$ with the frame-wise disparity at t for temporally consistent disparity \mathbf{d}_F^t , forming the final memory state \mathbf{m}_F^t at t .

scene and are thus not relevant anymore, leading to excess compute. Another common assumption is that only a single or few objects are in the scene, which restricts applicability. Our network can be seen as a “temporally local” SLAM system where only the immediately preceding frames are considered and no prior information of the scene is assumed.

3. Consistent Online Depth Network

The goal of this work is to estimate temporally consistent depth in dynamic scenes in an online setting. Let a memory state \mathbf{m} be a combination of per-pixel semantic and disparity information. Our network, shown in Fig. 2, consists of three sub-networks: 1) a *stereo* network \mathcal{N}_S that estimates the initial disparity and feature map \mathbf{m}_S^t on a per-frame basis at current time t , 2) a *motion* network \mathcal{N}_M that accounts for motion across frames by aligning the memory state from the previous frame with the current frame, denoted as \mathbf{m}_M^t , 3) a *fusion* network \mathcal{N}_F that promotes the temporal consistency between disparity estimates and produces the final memory state \mathbf{m}_F^t at time t . Each sub-network extracts or updates the input memory states. We introduce the high-level concepts of each sub-network in the following sections and detail the network designs in Appendix A.

3.1. Stereo Network

The objective of the stereo network is to extract semantic and disparity information from the current stereo image pair on a per-frame basis:

$$\mathbf{m}_S^t \leftarrow \mathcal{N}_S(\mathbf{L}^t, \mathbf{R}^t).$$

Here, the stereo network \mathcal{N}_s takes the current pair of left and right images $\mathbf{L}^t, \mathbf{R}^t$ as input. It extracts a set of feature maps from both images, and computes the disparity by finding matching between the feature maps, forming the initial memory state \mathbf{m}_S^t at time t . In this paper, we use one of

these recent networks, HITNet [24], as our building block to estimate per-frame disparity but note that our approach is agnostic to recent learning-based stereo solutions. In the subsequent sections, we discuss how to extend these stereo networks to stabilize the disparity prediction temporally.

3.2. Motion Network

The motion network aligns the previous memory state with that of the current frame in dynamic scenes. Let \mathbf{m}_F^{t-1} denote the preceding memory state from our online consistent depth network, and \mathbf{m}_S^t denote the current per-frame memory state from the stereo network. Both memory states contain the semantic and disparity information. Our motion network, as shown in Fig. 3a, aligns the previous memory state with the current frame based on both the current and previous memory states:

$$\mathbf{m}_M^t \leftarrow \mathcal{N}_M(\mathbf{m}_F^{t-1}, \mathbf{m}_S^t),$$

where \mathbf{m}_M^t is the memory state from $t - 1$ aligned to t , and \mathcal{N}_M is the motion network.

To perform such alignment, the inter-frame motion must be recovered. In a dynamic scene with camera motion and object motion/deformation, the motion prediction needs to be on a per-pixel level. Our motion network builds on top of RAFT3D [25] to predict a per-pixel SE3 transformation map \mathcal{T} . The motion is predicted using a GRU network and a Gauss-Newton optimization mechanism based on matching confidence for \mathcal{K} iterations. We detail differences between our motion network and RAFT3D in Appendix A.

Once the motion between frames is recovered, we project the previous memory state \mathbf{m}_F^{t-1} to the current frame [12] using differentiable rendering [22]:

$$\mathbf{m}_M^t \leftarrow \pi(\mathcal{T}\pi^{-1}(\mathbf{m}_F^{t-1})), \quad (1)$$

where π and π^{-1} are perspective and inverse perspective

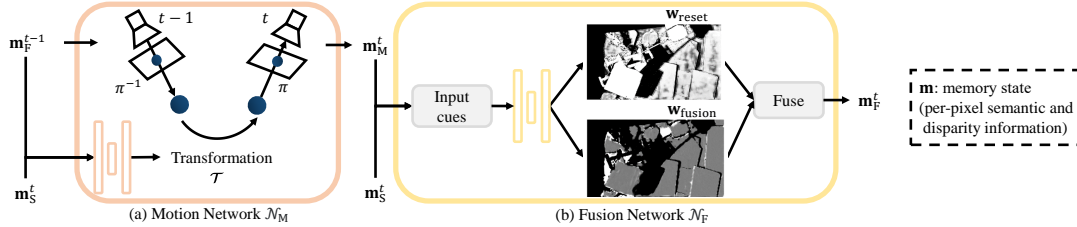


Figure 3. (a) The *motion* network \mathcal{N}_M lifts the preceding frame’s memory state \mathbf{m}_F^{t-1} to 3D via inverse perspective projection π^{-1} . It then computes a per-pixel SE3 transformation \mathcal{T} based on the previous memory state \mathbf{m}_F^{t-1} and current memory state \mathbf{m}_S^t , where \mathcal{T} aligns the observations at $t - 1$ to t . The motion network lastly projects the transformed predictions to 2D via perspective projection π , generating the aligned memory state \mathbf{m}_M^t . (b) The *fusion* network \mathcal{N}_F extracts input cues from the aligned memory state \mathbf{m}_M^t and per-frame memory state \mathbf{m}_S^t . It then estimates the reset and fusion weights, where $\mathbf{w}_{\text{reset}}$ removes outliers while $\mathbf{w}_{\text{fusion}}$ aggregates the predictions. The fusion network \mathcal{N}_F outputs the final memory state \mathbf{m}_F^t at t , with \mathbf{d}_F^t being the temporally consistent disparity estimate.

projection, respectively. The aligned memory state \mathbf{m}_M^t reside in the current camera coordinate frame and have pixel-wise correspondence with the current prediction, which enables temporal aggregation of disparity estimation. We also identify the regions in the current frame that is not visible in the previous frame as a binary visibility mask. Along with the flow magnitude/confidence from the motion estimation, the visibility mask is added to the memory state \mathbf{m}_M^t to be used later in the fusion network.

3.3. Fusion Network

The objective of the fusion network (Fig. 3b) is to promote temporal consistency by aggregating the disparity of the aligned memory state \mathbf{m}_M^t from the motion network and the disparity of the current memory state \mathbf{m}_S^t from the stereo network. The output of the fusion network is the final memory state \mathbf{m}_F^t at the current time t :

$$\mathbf{m}_F^t \leftarrow \mathcal{N}_F(\mathbf{m}_M^t, \mathbf{m}_S^t), \quad (2)$$

where \mathcal{N}_F is the fusion network.

3.3.1 Fusion Process

The temporally consistent disparity is obtained by fusing the aligned and current disparity estimates. Let \mathbf{d}_M^t be the disparity of the aligned memory state \mathbf{m}_M^t from the motion network and \mathbf{d}_S^t be the disparity of the current memory state \mathbf{m}_S^t from the stereo network. The fusion network computes a per-pixel reset weight $\mathbf{w}_{\text{reset}}$ and fusion weight $\mathbf{w}_{\text{fusion}}$. The fusion process of disparity estimates is formulated as:

$$\mathbf{d}_F^t = (1 - \mathbf{w}_{\text{reset}} \mathbf{w}_{\text{fusion}}) \mathbf{d}_S^t + \mathbf{w}_{\text{reset}} \mathbf{w}_{\text{fusion}} \mathbf{d}_M^t, \quad (3)$$

where \mathbf{d}_F^t is the fused disparity estimate. The final memory state \mathbf{m}_F^t is thus formed by the fused disparity \mathbf{d}_F^t and semantic information of stereo network’s memory state \mathbf{m}_S^t .

The intuition behind the fusion process is two-fold. First, it filters out outliers in a memory state using $\mathbf{w}_{\text{reset}}$. The outliers can be either induced by inaccurate disparity or motion

predictions. In our work, $\mathbf{w}_{\text{reset}}$ is supervised to identify the outliers whose errors are larger than the other disparity estimate with a threshold of τ_1 . Second, the fusion process encourages temporal consistency by fusing current disparity prediction with confident predictions propagated from previous frame using $\mathbf{w}_{\text{fusion}}$, similar to a voting-mechanism. When disparity estimates are considered to be equally good within a threshold τ_2 , the fusion network aggregates them with a regressed value between 0 and 1. The threshold τ_2 is a different threshold and $\tau_2 < \tau_1$, as reset weights should already reject the most significant outliers.

To determine the reset and fusion weights, we collect a set of input cues (Sec. 3.3.2) from the aligned memory state \mathbf{m}_M^t and the current memory state \mathbf{m}_S^t . The fusion network then uses convolution layers to process these input cues for regression. All convolution layers are shared between $\mathbf{w}_{\text{reset}}$ and $\mathbf{w}_{\text{fusion}}$ except for the final convolution layer. Both the reset and fusion weights are obtained through a Sigmoid layer, with their values bounded in the range of $(0, 1)$.

3.3.2 Input Cues

Disparity confidence First, the confidence of the current disparity \mathbf{d}_S^t and aligned disparity \mathbf{d}_M^t should guide the predictions of $\mathbf{w}_{\text{reset}}$ and $\mathbf{w}_{\text{fusion}}$. As disparities are computed mainly based on appearance similarity between the left and right images, we approximate the confidence of disparity prediction by computing the ℓ_1 distance between the left and right features extracted from stereo network given a disparity estimate. The confidence value is computed for each disparity estimate $\mathbf{d}_M^t, \mathbf{d}_S^t$ from the motion and stereo networks, respectively. For robustness against matching ambiguity, we additionally offset each disparity estimate by -1 and 1 to collect local confidence information, forming a 3 channel stereo matching confidence feature.

Self-correlation However, in the case of stereo occlusion, *i.e.* regions that are only visible in the left but not the right image, the disparity confidence based on appearance

similarity becomes ill-posed. Thus, we additionally use the local smoothness information as a cue. We implement a pixel-to-patch self-correlation (Fig. 4a) to approximate the local smoothness information, which computes the correlation between a pixel and its neighboring pixels in a local patch of size $W \times W$, forming a $W^2 - 1$ channel correlation feature. A dilation may be used to increase the receptive field. We apply the pixel-to-patch self-correlation for both disparity and semantic maps to acquire local depth and appearance smoothness.

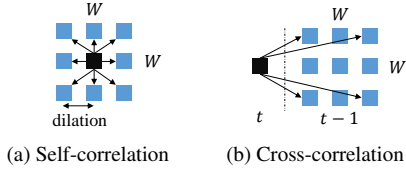


Figure 4. Pixel-to-patch correlation. The black pixel indicates the source pixel and the blue pixels indicate the attended pixels. (a) Self-correlation attends to a local patch except the source pixel. (b) Cross-correlation attends to a local patch in the previous frame. A dilation may be used to increase the receptive field.

Cross-correlation In the case of inaccurate motion predictions, the aligned memory state may contain wrong cross-frame correspondences. Therefore, the predictions in these regions need to be discarded as outliers. To promote such outlier rejection, the fusion network applies a pixel-to-patch cross-correlation (Fig. 4b) to evaluate the cross-frame disparity and appearance similarities. In cross-correlation, each pixel attends to a local $W \times W$ patch of the previous image centered at the same pixel location after motion correction, forming a W^2 correlation feature. Similar to self-correlation, a dilation may be used to increase the receptive field. In our implementation, we use the ℓ_1 distance for disparity and dot-products for appearance correlation.

Additional cues We observe that when the inter-frame motion is large, the motion estimate is less reliable and may thus result in wrong cross-frame correspondences. Therefore, we provide the flow magnitude and confidence as a motion cue. We additionally use the visibility mask from projection to identify the invalid regions. We lastly provide the semantic map to provide context information. We visualize different input cues in Appendix A.

3.4. Supervision

Stereo Network We supervise the stereo network on the per-frame disparity estimate \mathbf{d}_S^t against the ground truth disparity following [24], denoted as ℓ_S .

Motion Network We supervise the motion network on the transformation prediction \mathcal{T} , with an ℓ_1 loss imposed on its projected scene flow in image coordinates (*i.e.*, optical flow and disparity change) against the ground truth scene

flow following [25]. We denote the loss of the motion network as ℓ_M .

Fusion network We supervise the fusion network to promote temporal consistency of disparity estimates. We note that optimizing for disparity changes only may not be ideal, as errors in the previous frame will propagate to the current frame even if the predicted disparity change is correct. Therefore, we impose losses on both the disparity prediction \mathbf{d}_F^t , and the predicted weights $\mathbf{w}_{\text{reset}}, \mathbf{w}_{\text{fusion}}$.

We supervise the predicted disparity against the ground truth disparity using Huber loss [7], denoted as the disparity loss ℓ_{disp} . Further, we supervise the reset weights such that they reject the worse prediction between the current and previous disparity estimates:

$$\ell_{\text{reset}} = \begin{cases} \mathbf{w}_{\text{reset}}, & 1) \text{ if } e_M > e_S + \tau_1, \\ 1 - \mathbf{w}_{\text{reset}}, & 2) \text{ if } e_S > e_M + \tau_1, \\ 0, & 3) \text{ otherwise,} \end{cases} \quad (4)$$

where $e_M = |\mathbf{d}_M^t - \mathbf{d}_{\text{gt}}^t|$ is the error made by the aligned disparity and $e_S = |\mathbf{d}_S^t - \mathbf{d}_{\text{gt}}^t|$ is the error made by the current estimate against ground truth disparity \mathbf{d}_{gt}^t . Because $\mathbf{w}_{\text{reset}}$ rejects the aligned disparity estimate \mathbf{d}_M^t when its value is zero, we impose a loss such that it favors zero when e_M is worse as shown in condition 1) and favors one when e_S is worse as shown in condition 2). Otherwise, the loss is zero as shown in condition 3).

The fusion weights are supervised such that they aggregate the past two disparity estimates correctly:

$$\ell_{\text{fusion}} = \begin{cases} \mathbf{w}_{\text{fusion}}, & 1) \text{ if } e_M > e_S + \tau_2, \\ 1 - \mathbf{w}_{\text{fusion}}, & 2) \text{ if } e_S > e_M + \tau_2, \\ \alpha_{\text{reg}} \cdot |\mathbf{w}_{\text{fusion}} - 0.5|, & 3) \text{ otherwise.} \end{cases} \quad (5)$$

Different from the reset weights, the fusion weights are not only trained to identify the better estimate as shown in condition 1) and 2), but also trained with an additional regularization term such that the fusion weights are around 0.5 when both estimates are considered equally good as shown in condition 3).

The final loss for fusion network training is computed as:

$$\ell_F = \alpha_{\text{disp}} \ell_{\text{disp}} + \alpha_{\text{fusion}} \ell_{\text{fusion}} + \alpha_{\text{reset}} \ell_{\text{reset}}. \quad (6)$$

In our experiment, we set $\tau_1 = 5$, $\tau_2 = 1$, $\alpha_{\text{reg}} = 0.2$, and $\alpha_{\text{disp}} = \alpha_{\text{fusion}} = \alpha_{\text{reset}} = 1$ unless otherwise specified, which we find work well for our network.

4. Experimental Setup

4.1. Implementation Details

In our implementation, in the motion network we perform $\mathcal{K} = 16$ steps of incremental updates when datasets

contain large motion (e.g. FlyingThings3D [20] and KITTI Depth [27]) and $\mathcal{K} = 1$ otherwise (e.g. TartanAir [28] and MPI Sintel [3]). In the fusion network, we use a patch size $W = 3$ with a dilation of 2 for pixel-to-patch correlation to increase the receptive field. During training, we train with two frames unless otherwise specified. We apply the same random color augmentation and cropping of size 768×384 across temporal frames. We use a batch of 32 and Adam [9] as the optimizer on 8 Nvidia V100 GPUs.

4.2. Metrics

We propose to quantify the temporal inconsistency by a temporal end-point-error (TEPE) metric and the relative version (TEPE_r), which both compare the inter-frame disparity changes of estimated and ground truth given cross-frame correspondences:

$$\text{TEPE} = |\Delta d - \Delta d_{\text{gt}}|, \text{ and} \quad (7)$$

$$\text{TEPE}_r = \frac{\text{TEPE}}{|\Delta d_{\text{gt}}| + \epsilon}, \quad (8)$$

where $\epsilon = 1e-3$ to avoid division by zero. TEPE is generally proportional to the ground truth change magnitude and thus better reflects consistencies in pixels with large motion. TEPE_r better captures the consistencies of static pixels due to the $1/\epsilon$ weight. We also report $\delta_{3\text{px}}^1$ of 3px and $\delta_{100\%}^1$ of 100% as threshold metrics. Temporal metrics themselves can be limited as a network can be temporally stable but wrong. Therefore, we also report the per-pixel error of disparity estimates using EPE and threshold metric $\delta_{3\text{px}}^1$ of 3px. To quantify motion accuracy, we report the flow EPE (FEPE) on optical flow FEPE^{of} and scene flow FEPE^{sf}, and threshold metrics of 1px. For all results, we exclude pixels with extreme scene flow ($> 210\text{px}$) or disparity ($< 1\text{px}$ or $> 210\text{px}$) following [25].

5. Results and Discussion

We first show that current stereo depth estimation networks suffer from poor temporal stability quantitatively (Sec. 5.1). We show our network outperforms competing approaches across varied datasets with different training settings (Sec. 5.2–Sec. 5.4). We present ablation studies (Sec. 5.5), qualitative results (Sec. 5.6), and inference time (Sec. 5.7) to characterize our network. Lastly, limitations of the presented approach are discussed (Sec. 5.8).

5.1. Temporal Consistency Evaluation

We examine the temporal stability of stereo depth networks of different designs that operate on a per-frame basis.

Dataset FlyingThings3D finalpass [20] dataset is commonly used for training stereo networks, containing randomly moving rigid objects and camera motion. Thus, we use it to evaluate contemporary stereo depth algorithms.

Table 1. Temporal and per-pixel accuracy metrics of contemporary approaches evaluated on the FlyingThings3D dataset [20] with the official checkpoints when provided. †: We note that STTR only reports results in non-occluded region. As contemporary datasets [27, 28] do not have the occlusion information, evaluation of STTR on these datasets will not be representative due to the missing occlusion data. Thus, we use HITNet [24] as our baseline.

	TEPE ↓	$\delta_{3\text{px}}^1$ ↓	TEPE _r ↓	$\delta_{100\%}^1$ ↓	EPE ↓	$\delta_{3\text{px}}$ ↓
STTR [11] †	0.784	0.035	14.687	0.247	0.468	0.021
PSMNet [4]	1.414	0.041	20.869	0.401	1.119	0.046
GwcNet [6]	0.961	0.041	20.869	0.401	0.758	0.032
HITNet [24]	0.819	0.040	16.453	0.288	0.607	0.030

Results As shown in Tab. 1, all considered stereo networks have large TEPE and TEPE_r compared to the per-pixel EPE metric, with TEPE on the order of 1.3 times the EPE and more than 14 times the ground truth disparity change as implied by TEPE_r. This suggests that many contemporary stereo approaches suffer from poor temporal stability despite good per-pixel accuracy. In the following sections, we demonstrate that our network improves the temporal stability of per-frame networks and outperforms competing approaches.

5.2. Pre-training on FlyingThings3D

Training setup We use HITNet [24] as our stereo network and freeze its parameters for fair comparison. To be robust against noise in stereo estimates, we train the motion sub-network taking stereo predictions as input for 25000 iterations. We then pre-train the fusion network for 12500 iterations using the stereo and motion networks’ output. We follow the official split and report results over the whole sequence (10 frames) for each scene.

Results Sharing the same stereo network parameters as HITNet [24], our consistent online depth network outperforms the baseline HITNet [24] and Kalman filter [29] in all metrics as shown in Tab. 2. We note that TEPE decreases from 0.819 to 0.752 and TEPE_r decreases from 16.453 to 14.867, suggesting that the temporal consistency improves for pixels with large and small motion. Furthermore, the per-pixel disparity accuracy metric EPE also decreases from 0.607 to 0.599, in contrast to Kalman filter which leads to worse EPE. The result indicates that our network achieves better stability across frames by pushing predictions towards the ground truth instead of propagating errors in time.

Table 2. Results on the FlyingThings3D dataset [20]. Our network shares the same network parameters with the baseline [24].

	TEPE ↓	$\delta_{3\text{px}}^1$ ↓	TEPE _r ↓	$\delta_{100\%}^1$ ↓	EPE ↓	$\delta_{3\text{px}}$ ↓
Baseline [24]	0.819	0.040	16.453	0.288	0.607	0.030
Kalman filter [29]	0.800	0.040	15.462	0.228	0.611	0.030
Ours	0.752	0.034	14.867	0.212	0.599	0.029

Table 3. Benchmark result on TartanAir [28] and KITTI Depth [27] datasets. Ours: baseline stereo model attached with pre-trained motion and fusion networks from FlyingThings3D dataset [20]. +M: fine-tune motion network. +M+F: fine-tune motion and fusion networks.

	TEPE ↓	δ_{3px}^i ↓	TEPE _r ↓	$\delta_{100\%}^i$ ↓	EPE ↓	δ_{3px} ↓	FEPE ^{of} ↓	δ_{1px}^{of} ↓	FEPE ^{sf} ↓	δ_{1px}^{sf} ↓
TartanAir dataset [28]										
Baseline [24]	0.876	0.053	9.039	0.339	0.934	0.055	N/A			
Kalman Filter [29]	0.829	0.053	7.501	0.252	0.935	0.055	N/A			
Ours	0.813	0.049	6.534	0.256	0.978	0.058	2.455	0.469	2.624	0.486
Ours (+M)	0.760	0.046	6.368	0.242	0.929	0.054	1.139	0.228	1.264	0.241
Ours (+M+F)	0.751	0.045	6.206	0.240	0.904	0.053	1.129	0.225	1.253	0.238
KITTI Depth dataset [27]										
Baseline [24]	0.289	0.001	3.630	0.156	0.423	0.004	N/A			
Kalman Filter [29]	0.278	0.001	2.615	0.125	0.431	0.005	N/A			
Ours	0.252	0.001	2.502	0.123	0.428	0.004	0.423	0.063	0.548	0.112
Ours (+M)	0.248	0.001	2.155	0.123	0.427	0.004	0.245	0.020	0.380	0.058
Ours (+M+F)	0.258	0.001	2.764	0.132	0.418	0.003	0.245	0.020	0.380	0.058

5.3. Benchmark Results

We then benchmark our network with fine-tuning on two large datasets – TartanAir [28] and KITTI Depth [27].

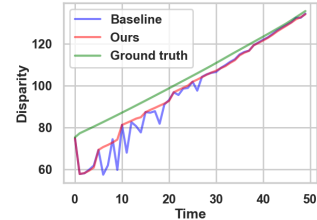
Dataset TartanAir is a synthetic dataset with simulated drone motions in different scenes, which contain dynamic objects and different weather conditions such as raining. We use 15 scenes (219434 images) for training, 1 scene for validation (6607 images) and 1 scene (5915 images) for testing.

KITTI Depth has footage of real-world driving scenes, where ground truth is acquired from LiDAR. We follow the official split and train our network on 57 video sequences (38331 images), validate on 1 video sequence (1100 images), and test on 13 video sequences (3426 images).

Training Setup We first fine-tune the per-frame stereo model dataset for 12500 iterations. For fair comparison, we report the results of the same per-frame stereo model attached with the pre-trained motion/fusion networks from FlyingThings3D (Ours). We then report results with motion/fusion networks also fine-tuned for 12500 iterations and 6250 iterations respectively (+M and +M+F). All learning rates are linearly decayed from $2e-5$. For long sequences (several thousands), we chunk the video into subsequences of 50 frames following [3]. Due to the sparsity of KITTI Depth dataset (approximately 4% valid data per image), we find the number of supervision pixels for reset and fusion weights are often 1 or 2 pixels per image, which leads to ineffective training (quantitative results in Appendix B). Therefore, we set $\alpha_{reset} = \alpha_{fusion} = 0.0$ as a compromise. We report results of end-to-end training in Appendix C.

Results As shown in Tab. 3, our network consistently outperforms the baseline [24] and Kalman filter [29] in terms of temporal metrics in both datasets, even with pre-trained motion/fusion networks (Ours). The performance improvement without fine-tuning motion/fusion networks may be attributed to the outlier rejection mechanism of our fusion network (visualization in Appendix D). Even if the motion estimate contains errors, our fusion network can reject outliers resulting in improved performance. As we fine-

Figure 5. Disparity estimate of baseline [24] and our network against ground truth tracing the same point across time.



tune the motion/fusion networks (+M and +M+F), our network outperforms competing approaches in all metrics, except when fine-tuning the fusion network on KITTI Depth. Fine-tuning the fusion network (+M+F) leads to slightly worse temporal performance than without (+M), which is attributed to the missing supervision on w_{reset} and w_{fusion} .

5.4. Zero-shot Generalization

Dataset We report zero-shot generalization results of our pre-trained network from FlyingThings3D on the TartanAir, KITTI Depth and MPI Sintel dataset finalpass [3]. MPI Sintel contains animated characters with deformation. It contains 23 video sequences, totaling 1064 images.

Results As shown in Tab. 4, our model is able to generalize well onto a new data domain and significantly improves over the baseline [24] and Kalman filter [29] in terms of temporal metrics, up to 63% (TEPE_r of KITTI Depth: from 95.691 to 34.741). Our network also outperforms the competing approaches in terms of EPE, with the only exception being the TartanAir dataset (1.837 vs. 1.833 vs. 1.861).

Table 4. Zero-shot generalization experiments on TartanAir [28], KITTI Depth [27] and MPI Sintel [3] datasets. All networks are trained only on FlyingThings3D [20].

	TEPE ↓	δ_{3px}^i ↓	TEPE _r ↓	$\delta_{100\%}^i$ ↓	EPE ↓	δ_{3px} ↓
TartanAir dataset [28]						
Baseline [24]	1.387	0.091	16.501	0.458	1.837	0.126
Kalman Filter [29]	1.325	0.091	14.452	0.359	1.833	0.126
Ours	1.211	0.077	11.046	0.347	1.861	0.129
KITTI Depth dataset [27]						
Baseline [24]	3.627	0.325	95.691	0.594	7.314	0.481
Kalman Filter [29]	3.565	0.324	93.293	0.561	7.311	0.480
Ours	1.983	0.134	34.741	0.372	6.833	0.426
MPI Sintel dataset [3]						
Baseline [24]	2.621	0.127	298.674	0.515	5.028	0.199
Kalman Filter [29]	2.583	0.126	287.456	0.460	5.027	0.199
Ours	2.270	0.092	191.445	0.439	5.009	0.199

5.5. Ablation Experiments

We conduct experiments on the FlyingThings3D dataset [20] to ablate the effectiveness of different components.

5.5.1 Motion Network

We evaluate the motion accuracy of our motion network because accurate motion prediction is critical to our process. As our motion network is built on top of RAFT3D [25], we compare the performance of our motion network and RAFT3D in Tab. 5. We evaluate the performance in two settings, 1) taking the ground truth disparity as input and 2) taking the noisy stereo disparity estimates as input. For fair comparison, we re-train RAFT3D using our training setup and report its result. As shown, our network performs better in both FEPE^{of} and FEPE^{sf} regardless of the input type, with only 1/5-th of the parameters of RAFT3D.

Table 5. Ablation study of the motion network. GT: ground truth disparity as input. S: stereo network disparity estimates as input. ‡: official checkpoint.

	FEPE ^{of} ↓	δ_{1px}^{of} ↓	FEPE ^{sf} ↓	δ_{1px}^{sf} ↓	Parameters ↓
RAFT3D (GT) [25] ‡	2.145	0.131	2.177	0.138	45.0M
RAFT3D (GT) [25]	1.808	0.133	1.847	0.141	45.0M
Ours (GT)	1.754	0.127	1.793	0.135	8.5M
RAFT3D (S) [25]	2.458	0.149	2.514	0.158	45.0M
Ours (S)	1.902	0.134	1.949	0.142	8.5M

5.5.2 Fusion Network

We summarize the key ablation experiments in Tab. 6 and provide additional results in Appendix E.

a) Reset weights In theory, only one regression weight is needed between two estimates. However, we find that additional reset weights improve performance. This may be attributed to the difference in supervision where reset weights are trained to estimate binary values for outlier detection, while fusion weights are trained for aggregation.

b) Fusion input cues Other than the disparity confidence, self- and cross-correlation, we incrementally add the flow confidence/magnitude (+FL), visibility mask (+V) and semantic map (+SM) to the fusion networks. We find that the metrics improve marginally with additional inputs.

c) Number of training frames During training, by default we train with two frames. We extend training frames to three/four frames to approximate the inference process, where preceding predictions are from fusion instead of stereo networks. We find that the fusion network consistently benefits from increasing number of training frames. However, this elongates training time proportionally.

d-e) Empirical best case We provide an empirical study of the “best case” of either motion or fusion network. For \mathcal{N}_M in d), we use ground truth scene flow and set flow confidence to one. For \mathcal{N}_F in e), we always pick the better disparity estimates pixel-wise between current/aligned prediction given ground truth. Perfect motion d) leads to substantial reduction in TEPE_r while perfect fusion e) leads to substantial reduction in TEPE. In both cases, EPE are also smaller.

While our network performs well compared to conventional techniques, advancing the motion or fusion modules has the potential to substantially improve stability.

Table 6. Ablation study of the fusion network. Underline: base configuration. *Italic*: final configuration.

		TEPE ↓	δ_{3px}^t ↓	TEPE _r ↓	$\delta_{100\%}^t$ ↓	EPE ↓	δ_{3px} ↓
a) Reset weight	×	0.783	0.036	15.953	0.217	0.618	0.030
	✓	0.756	0.035	15.013	0.211	0.604	0.029
b) Fusion input cues	+FL	0.763	0.035	15.103	0.211	0.604	0.029
	+V	0.758	0.035	15.082	0.210	0.605	0.029
	<u>+SM</u>	0.756	0.035	15.013	0.211	0.604	0.029
c) Number of training frames	<u>2</u>	0.756	0.035	15.013	0.211	0.604	0.029
	3	0.753	0.035	14.942	0.211	0.600	0.029
	4	0.752	<i>0.034</i>	<i>14.867</i>	<i>0.212</i>	<i>0.599</i>	<i>0.029</i>
d) Empirical best \mathcal{N}_M		0.879	0.043	5.401	0.125	0.571	0.027
e) Empirical best \mathcal{N}_F		0.529	0.025	9.936	0.214	0.455	0.021

5.6. Qualitative Visualization

We provide visualizations in 3D in the video supplement, including results of additional footage collected in indoor environments and medical scenes. In Fig. 5, we visualize the improvement of our proposed network over the baseline [24]. The disparity of a point is traced across frames. We find that predictions from our network do not exhibit the high frequency jitter of the baseline, suggesting the better temporal consistency of our network.

5.7. Inference Speed and Number of Parameters

The inference speed of our network on images of resolution 640×512 with $\mathcal{K} = 1$ is 25 FPS (stereo 26ms, motion 13ms, fusion 0.3ms) on an Nvidia Titan RTX GPU. The total number of parameters is 9.3M (stereo 0.6M, motion 8.5M and fusion 0.2M). Compared to the baseline [24], the overhead is mainly introduced by the motion network.

5.8. Limitations

While our approach outperforms competing methods across datasets, we recognize that there is still a gap between our network and the empirical best cases in Sec. 5.5.2. Furthermore, when both current/previous frame estimates are wrong, our network cannot correct the error as the weights between current and previous estimates in the fusion process are bounded to (0, 1). Lastly, we design our network to look at the immediate preceding frame only. Future work may extend to multiple past frames.

6. Conclusions

We present a general framework to produce temporally consistent depth estimation for dynamic scenes in an online setting. Our approach builds on contemporary per-frame stereo depth approaches and shows superior performance across different benchmarks. Future work may extend upon our motion or fusion network for better performance.

References

- [1] Alex M Andrew. Multiple view geometry in computer vision. *Kybernetes*, 2001. [1](#)
- [2] Aseem Behl, Despoina Paschalidou, Simon Donn e, and Andreas Geiger. Pointflownet: Learning representations for rigid motion estimation from point clouds. In *Proceedings of the IEEE/CVF Conference on Computer Vision and Pattern Recognition*, pages 7962–7971, 2019. [2](#)
- [3] D. J. Butler, J. Wulff, G. B. Stanley, and M. J. Black. A naturalistic open source movie for optical flow evaluation. In A. Fitzgibbon et al. (Eds.), editor, *European Conf. on Computer Vision (ECCV)*, Part IV, LNCS 7577, pages 611–625. Springer-Verlag, Oct. 2012. [2](#), [6](#), [7](#)
- [4] Jia-Ren Chang and Yong-Sheng Chen. Pyramid stereo matching network. In *Proceedings of the IEEE Conference on Computer Vision and Pattern Recognition*, pages 5410–5418, 2018. [1](#), [2](#), [6](#)
- [5] Chanho Eom, Hyunjong Park, and Bumsub Ham. Temporally consistent depth prediction with flow-guided memory units. *IEEE Transactions on Intelligent Transportation Systems*, 21(11):4626–4636, 2019. [2](#)
- [6] Xiaoyang Guo, Kai Yang, Wukui Yang, Xiaogang Wang, and Hongsheng Li. Group-wise correlation stereo network. In *Proceedings of the IEEE/CVF Conference on Computer Vision and Pattern Recognition*, pages 3273–3282, 2019. [1](#), [2](#), [6](#)
- [7] Peter J Huber. Robust estimation of a location parameter. In *Breakthroughs in statistics*, pages 492–518. Springer, 1992. [5](#)
- [8] Matthias Innmann, Michael Zollh ofer, Matthias Nie bner, Christian Theobalt, and Marc Stamminger. Volumedeform: Real-time volumetric non-rigid reconstruction. *ArXiv*, abs/1603.08161, 2016. [2](#)
- [9] Diederik P Kingma and Jimmy Ba. Adam: A method for stochastic optimization. *arXiv preprint arXiv:1412.6980*, 2014. [6](#)
- [10] Johannes Kopf, Xuejian Rong, and Jia-Bin Huang. Robust consistent video depth estimation. In *Proceedings of the IEEE/CVF Conference on Computer Vision and Pattern Recognition*, pages 1611–1621, 2021. [2](#)
- [11] Zhaoshuo Li, Xingtong Liu, Nathan Drenkow, Andy Ding, Francis X Creighton, Russell H Taylor, and Mathias Unberath. Revisiting stereo depth estimation from a sequence-to-sequence perspective with transformers. In *Proceedings of the IEEE/CVF International Conference on Computer Vision*, pages 6197–6206, 2021. [1](#), [2](#), [6](#)
- [12] Zhaoshuo Li, Amirreza Shaban, Jean-Gabriel Simard, Dinesh Rabindran, Simon DiMaio, and Omid Mohareri. A robotic 3d perception system for operating room environment awareness. *arXiv preprint arXiv:2003.09487*, 2020. [3](#)
- [13] Chao Liu, Jinwei Gu, Kihwan Kim, Srinivasa G Narasimhan, and Jan Kautz. Neural rgb (r) d sensing: Depth and uncertainty from a video camera. In *Proceedings of the IEEE/CVF Conference on Computer Vision and Pattern Recognition*, pages 10986–10995, 2019. [1](#), [2](#)
- [14] Xingyu Liu, Charles R Qi, and Leonidas J Guibas. Flownet3d: Learning scene flow in 3d point clouds. In *Proceedings of the IEEE/CVF Conference on Computer Vision and Pattern Recognition*, pages 529–537, 2019. [2](#)
- [15] Xiaoxiao Long, Lingjie Liu, Wei Li, Christian Theobalt, and Wenping Wang. Multi-view depth estimation using epipolar spatio-temporal networks. In *Proceedings of the IEEE/CVF Conference on Computer Vision and Pattern Recognition*, pages 8258–8267, 2021. [1](#), [2](#)
- [16] Yonghao Long, Zhaoshuo Li, Chi Hang Yee, Chi Fai Ng, Russell H Taylor, Mathias Unberath, and Qi Dou. E-dssr: Efficient dynamic surgical scene reconstruction with transformer-based stereoscopic depth perception. In *International Conference on Medical Image Computing and Computer-Assisted Intervention*, pages 415–425. Springer, 2021. [2](#)
- [17] Xuan Luo, Jia-Bin Huang, Richard Szeliski, Kevin Matzen, and Johannes Kopf. Consistent video depth estimation. *ACM Transactions on Graphics (TOG)*, 39(4):71–1, 2020. [2](#)
- [18] Wei-Chiu Ma, Shenlong Wang, Rui Hu, Yuwen Xiong, and Raquel Urtasun. Deep rigid instance scene flow. In *Proceedings of the IEEE/CVF Conference on Computer Vision and Pattern Recognition*, pages 3614–3622, 2019. [2](#)
- [19] Sergey Matyunin, Dmitriy Vatolin, Yury Berdnikov, and Maxim Smirnov. Temporal filtering for depth maps generated by kinect depth camera. In *2011 3DTV Conference: The True Vision-Capture, Transmission and Display of 3D Video (3DTV-CON)*, pages 1–4. IEEE, 2011. [2](#)
- [20] Nikolaus Mayer, Eddy Ilg, Philip Hausser, Philipp Fischer, Daniel Cremers, Alexey Dosovitskiy, and Thomas Brox. A large dataset to train convolutional networks for disparity, optical flow, and scene flow estimation. In *Proceedings of the IEEE conference on computer vision and pattern recognition*, pages 4040–4048, 2016. [2](#), [6](#), [7](#)
- [21] Richard A Newcombe, Dieter Fox, and Steven M Seitz. Dynamicfusion: Reconstruction and tracking of non-rigid scenes in real-time. In *Proceedings of the IEEE conference on computer vision and pattern recognition*, pages 343–352, 2015. [2](#)
- [22] Nikhila Ravi, Jeremy Reizenstein, David Novotny, Taylor Gordon, Wan-Yen Lo, Justin Johnson, and Georgia Gkioxari. Accelerating 3d deep learning with pytorch3d. *arXiv:2007.08501*, 2020. [3](#)
- [23] Denis Tananaev, Huizhong Zhou, Benjamin Ummenhofer, and Thomas Brox. Temporally consistent depth estimation in videos with recurrent architectures. In *Proceedings of the European Conference on Computer Vision (ECCV) Workshops*, pages 0–0, 2018. [2](#)
- [24] Vladimir Tankovich, Christian Hane, Yinda Zhang, Adarsh Kowdle, Sean Fanello, and Sofien Bouaziz. Hitnet: Hierarchical iterative tile refinement network for real-time stereo matching. In *Proceedings of the IEEE/CVF Conference on Computer Vision and Pattern Recognition*, pages 14362–14372, 2021. [1](#), [2](#), [3](#), [5](#), [6](#), [7](#), [8](#)
- [25] Zachary Teed and Jia Deng. Raft-3d: Scene flow using rigid-motion embeddings. In *Proceedings of the IEEE/CVF Conference on Computer Vision and Pattern Recognition*, pages 8375–8384, 2021. [2](#), [3](#), [5](#), [6](#), [8](#)
- [26] Iraklis Tsekourakis and Philippos Mordohai. Measuring the effects of temporal coherence in depth estimation for dy-

- dynamic scenes. In *Proceedings of the IEEE/CVF Conference on Computer Vision and Pattern Recognition Workshops*, pages 0–0, 2019. [2](#)
- [27] Jonas Uhrig, Nick Schneider, Lukas Schneider, Uwe Franke, Thomas Brox, and Andreas Geiger. Sparsity invariant cnns. In *2017 international conference on 3D Vision (3DV)*, pages 11–20. IEEE, 2017. [2](#), [6](#), [7](#)
- [28] Wenshan Wang, DeLong Zhu, Xiangwei Wang, Yaoyu Hu, Yuheng Qiu, Chen Wang, Yafei Hu, Ashish Kapoor, and Sebastian Scherer. Tartanair: A dataset to push the limits of visual slam. In *2020 IEEE/RSJ International Conference on Intelligent Robots and Systems (IROS)*, pages 4909–4916. IEEE, 2020. [2](#), [6](#), [7](#)
- [29] Greg Welch, Gary Bishop, et al. An introduction to the kalman filter. 1995. [2](#), [6](#), [7](#)
- [30] Gengshan Yang and Deva Ramanan. Upgrading optical flow to 3d scene flow through optical expansion. In *Proceedings of the IEEE/CVF Conference on Computer Vision and Pattern Recognition*, pages 1334–1343, 2020. [2](#)
- [31] Tao Yu, Kaiwen Guo, Feng Xu, Yuan Dong, Zhaoqi Su, Jianhui Zhao, Jianguo Li, Qionghai Dai, and Yebin Liu. Body-fusion: Real-time capture of human motion and surface geometry using a single depth camera. *2017 IEEE International Conference on Computer Vision (ICCV)*, pages 910–919, 2017. [2](#)
- [32] Haokui Zhang, Chunhua Shen, Ying Li, Yuanzhouhan Cao, Yu Liu, and Youliang Yan. Exploiting temporal consistency for real-time video depth estimation. In *Proceedings of the IEEE/CVF International Conference on Computer Vision*, pages 1725–1734, 2019. [2](#)
- [33] Zhoutong Zhang, Forrester Cole, Richard Tucker, William T Freeman, and Tali Dekel. Consistent depth of moving objects in video. *ACM Transactions on Graphics (TOG)*, 40(4):1–12, 2021. [2](#)